A Galerkin-RBF approach for the streamfunction-vorticity-temperature formulation of natural convection in 2D enclosured domains

D. Ho-Minh, N. Mai-Duy and T. Tran-Cong
Computational Engineering and Science Research Centre (CESRC)
Faculty of Engineering and Surveying (FoES)
The University of Southern Queensland, Toowoomba, QLD 4350, Australia.

Abstract: This paper reports a new discretisation technique for the streamfunction-vorticity-temperature ($\psi-\omega-T$) formulation governing natural convection defined in 2D enclosured domains. The proposed technique combines strengths of three schemes, i.e. smooth discretisations (Galerkin formulation), powerful high-order approximations (one-dimensional integrated radial-basis-function networks) and pressure-free low-order system ($\psi-\omega-T$ formulation). In addition, a new effective way of deriving computational boundary conditions for the vorticity is proposed. Two benchmark test problems, namely free convection in a square slot and a concentric annulus, are considered, where a convergent solution for the former is achieved up to the Rayleigh number of 10^8.

Keywords: Integrated RBFNs, Galerkin approach, streamfunction-vorticity-temperature formulation, natural convection.

1 Introduction

Radial-basis-function networks (RBFNs) have been widely used in the area of numerical analysis. In the context of the numerical solution of partial-differential equations (PDEs), RBFNs have received a great deal of attention from both scientific and engineering research communities over the last 15 years. The first report on this subject was presented by Kansa (1990). For Kansa's method, a function is first represented by an RBFN which is then differentiated to obtain approximate expressions for its derivative functions. On the other hand, to avoid the reduction in convergence rate caused by differentiation, Mai-Duy and Tran-Cong (2001) proposed an indirect/integrated RBFN (IRBFN) approach in which the highest-order derivatives in the PDE are first decomposed into RBFs, and their lower-order derivatives and the function itself are then obtained through integration. Numerical experiments (e.g. [Mai-Duy and Tran-Cong (2001, 2003)]) showed that IRBFN collocation methods yield better accuracy than differentiated RBFN (DRBFN) ones for both the representation of functions and the solution of PDEs. Since the RBF interpolation matrix is fully populated and its condition number grows rapidly with respect to the increase of RBF centres and/or widths [Schaback (1995)], global RBF methods are only able to work with relatively-low num-

bers of points. To overcome this drawback, several treatments have been proposed, e.g. preconditioning schemes [Kansa and Hon (2000); Ling and Kansa (2005)], local approximations [Shu, Ding, and Yeo (2005); Shan, Shu, and Lu (2008); Kosec and Sarler (2008)] and domain decompositions [Ingber, Chen, and Tanski (2004); Divo and Kassab (2006)]. In the context of IRBFNs, collocation schemes, based on one-dimensional (1D) IRBFNs and Cartesian grids, for the solution of 2D elliptic PDEs were reported in, e.g. [Mai-Duy and Tran-Cong (2007)]. The RBF approximations at a grid node involve only points that lie on the grid lines intersecting at that point rather than the whole set of nodes. As a result, the construction process is conducted for a series of small matrices rather than for a large single matrix ("local" approximation).

Apart from the point-collocation formulation, RBFs have been employed as trial functions in other formulations such as those associated with the finite-element, finite-volume and boundary-element methods. Works in this research direction include [Atluri, Han, and Rajendran (2004); Wang and Wang (2006); Wang, Lim, Khoo, and Wang (2007); Sellountos and Sequeira (2008); Orsini, Power, and Morvan (2008); Mohammadi (2008); Sellountos, Sequeira, and Polyzos (2009)].

Very recently, a discretisation technique, based on 1D-IRBFNs and Galerkin approximations, for the solution of linear Poisson equations was reported in [Mai-Duy and Tran-Cong (2009)]. The boundary conditions are satisfied in a local sense using the point collocation formulation, and the solution to the problem is satisfied in a global sense using the Galerkin formulation. The use of integration to construct the approximations generates some additional coefficients (i.e. the constants of integration) that can be exploited for the effective implementation of Neumann and multiple boundary conditions. The resultant system of algebraic equations is often symmetric and has a relatively-low condition number, which facilitate the employment of much larger numbers of nodes. Numerical results showed that this technique yields accurate results, high rates of convergence, and especially similar levels of accuracy for both types of boundary condition (i.e. Dirichlet only and Dirichlet-Neumann).

Natural convection, which occurs in many engineering applications, presents a strong coupling of heat transfer and fluid flow. Problems of this type have been extensively studied by means of experimental and numerical simulations. Natural convection in a square slot and in an annulus have been widely considered as two benchmark problems for the testing of new numerical schemes in CFD. For the case of high Rayleigh (Ra) numbers, very thin boundary layers are formed, which presents a great challenge for any numerical method. As a result, to simulate such cases, low-order techniques such as finite-difference methods (FDMs) (e.g. [Saitoh and Hirose (1989)]) and finite-element methods (FEMs) (e.g [Manzari (1999); Wan, Patnail, and Wei (2001); Mayne, Usmani, and Crapper (2000, 2001)]) typically require a very fine mesh. This requirement is alleviated by employing high-order methods such as pseudo-spectral methods (e.g. [Quéré (1991)]), discrete singular convolu-

tion (DSC) methods (e.g. [Wan, Patnail, and Wei (2001)]), meshless diffuse approximation methods (DAMs) (e.g. [Sadat and Couturier (2000)]), and mesh-free local RBF collocation methods (RBFCM) (e.g. [Sarler (2005); Kosec and Sarler (2007)]). However, in general, there still exist some difficult problems associated with convergence (e.g. relatively-few reports for the case of $Ra > 10^6$ for natural convection in a square slot) and accuracy (e.g. some discrepancies in the prediction of the Nusselt number among published works).

In this paper, we present a new high-order Galerkin technique, which is based on 1D-IRBFNs and Cartesian grids, for the simulation of natural convection in two dimensions. Advantages of using 1D-IRBFNs over 2D-IRBFNs are (i) the construction cost is much lower ("local" approximations), (ii) the matrix condition number is greatly improved and (iii) the system matrix becomes sparse. However, their disadvantage is that tensor products are required to construct the approximations over the whole domain. Coordinate transformations are thus needed to handle nonrectangular domains. Unlike FD and Chebyshev interpolation schemes, IRBFNs can work well with nonuniform and uniform Cartesian grids. The streamfunction-vorticity-temperature ($\psi - \omega - T$) formulation will be adopted here to take the following advantages: (a) the continuity equation is satisfied automatically, (b) its implementation is easier as the pressure variable is eliminated, and (c) its matrix condition number (second-order system) is significantly improved over that of the streamfunction-temperature formulation (fourth-order system). However, when using the $\psi - \omega - T$ formulation, the classical difficulties lie in the treatment of boundary condition for the vorticity. A new effective boundary scheme is proposed, where computational boundary conditions for the vorticity are derived in a precise manner (i.e. approximations used on the boundary have the same order as those for the interior points, and derivative values of the streamfunction on the boundary are incorporated into the IRBFN approximations in an exact manner). The present method is verified through the simulation of natural convection in 2D enclosed domains. Two different geometries are considered: (i) a square slot and (ii) a concentric annulus. It will be shown that convergent solutions are achieved for very high values of the Rayleigh number (i.e. up to 10^8 for the former and 7×10^4 for the latter). Numerical results obtained are compared with those by other techniques available in the literature.

The remainder of this paper is organised as follows. Section 2 briefly describes the governing equations in both Cartesian and cylindrical coordinates. Our proposed technique is presented in detail in section 3, including 1D-IRBFN representations of the field variables, Galerkin discretisations of the PDEs and a new treatment for the vorticity boundary condition. In section 4, the technique is verified through the simulation of several benchmark test problems. Section 5 concludes the paper.

2 Governing equations

In this study, the governing equations are taken as the streamfunction-vorticity-temperature formulation. Both Cartesian and cylindrical coordinate systems are employed here. Using

the Boussinesq approximation, the 2D dimensionless forms of the governing equations can be written as

$$\frac{\partial^2\psi}{\partial x^2}+\frac{\partial^2\psi}{\partial y^2} = -\omega, \tag{1}$$

$$\frac{\partial\omega}{\partial t}+u\frac{\partial\omega}{\partial x}+v\frac{\partial\omega}{\partial y} = \sqrt{\frac{Pr}{Ra}}\left(\frac{\partial^2\omega}{\partial x^2}+\frac{\partial^2\omega}{\partial y^2}\right)+\frac{\partial T}{\partial x}, \tag{2}$$

$$\frac{\partial T}{\partial t}+u\frac{\partial T}{\partial x}+v\frac{\partial T}{\partial y} = \frac{1}{\sqrt{RaPr}}\left(\frac{\partial^2 T}{\partial x^2}+\frac{\partial^2 T}{\partial y^2}\right), \tag{3}$$

for Cartesian coordinates, where

$$u=\frac{\partial\psi}{\partial y}, \quad v=-\frac{\partial\psi}{\partial x},$$

and

$$\frac{\partial^2\psi}{\partial r^2}+\frac{1}{r}\frac{\partial\psi}{\partial r}+\frac{1}{r^2}\frac{\partial^2\psi}{\partial\theta^2} = -\omega, \tag{4}$$

$$\frac{\partial\omega}{\partial t}+\left(u\frac{\partial\omega}{\partial r}+\frac{v}{r}\frac{\partial\omega}{\partial\theta}\right) = \sqrt{\frac{Pr}{Ra}}\left(\frac{\partial^2\omega}{\partial r^2}+\frac{1}{r}\frac{\partial\omega}{\partial r}+\frac{1}{r^2}\frac{\partial^2\omega}{\partial\theta^2}\right) - \left(\sin\theta\frac{\partial T}{\partial r}+\frac{1}{r}\cos\theta\frac{\partial T}{\partial\theta}\right), \tag{5}$$

$$\frac{\partial T}{\partial t}+\left(u\frac{\partial T}{\partial r}+\frac{v}{r}\frac{\partial T}{\partial\theta}\right) = \frac{1}{\sqrt{RaPr}}\left(\frac{\partial^2 T}{\partial r^2}+\frac{1}{r}\frac{\partial T}{\partial r}+\frac{1}{r^2}\frac{\partial^2 T}{\partial\theta^2}\right), \tag{6}$$

for cylindrical coordinates, where

$$u=\frac{1}{r}\frac{\partial\psi}{\partial\theta}, \quad v=-\frac{\partial\psi}{\partial r}.$$

In Eq. 3 and Eq. 6, Pr and Ra are the Prandtl and Rayleigh numbers defined as $Pr=\nu/\alpha$ and $Ra=\beta g\Delta T L^3/\alpha\nu$, respectively in which ν is the kinematic viscosity, α the thermal diffusivity, β the thermal expansion coefficient, g the gravity, and L and ΔT the characteristic length and temperature difference, respectively. In this dimensionless scheme, the velocity scale is taken as $U=\sqrt{gL\beta\Delta T}$ for the purpose of balancing the buoyancy and inertial forces.

The given velocity boundary conditions, u and v, can be transformed into two boundary conditions on the streamfunction and its normal derivative

$$\psi = A, \tag{7}$$

$$\frac{\partial\psi}{\partial n} = B, \tag{8}$$

where n is the direction normal to the boundary, and A and B given functions which are simply zero here. For problems presented in this study, the boundary conditions for the energy equation are prescribed with both Dirichlet and Neumann types.

3 The proposed technique

The problem domain is represented by a Cartesian grid. On each grid line, 1D-IRBFNs are employed to approximate the field variables (i.e. ψ, ω and T). The governing equations are discretised by means of Galerkin approximations (i.e. the residuals are set to zero in the mean). Vorticity boundary conditions are derived globally.

3.1 One-dimensional IRBFN representations of the field variables

The system of PDEs under consideration here is of second order. Consider a η grid line. Applying the integral RBF scheme [Mai-Duy and Tran-Cong (2003)], a function f and its derivatives with respect to η can be represented as follows

$$\frac{d^2 f(\eta)}{d\eta^2} = \sum_{i=1}^{N_\eta} w_i g_i(\eta) = \sum_{i=1}^{N_\eta} w_i I_i^{(2)}(\eta), \tag{9}$$

$$\frac{df(\eta)}{d\eta} = \sum_{i=1}^{N_\eta} w_i I_i^{(1)}(\eta) + c_1, \tag{10}$$

$$f(\eta) = \sum_{i=1}^{N_\eta} w_i I_i^{(0)}(\eta) + c_1\eta + c_2, \tag{11}$$

where N_η is the number of nodes on the grid line, $\{w_i\}_{i=1}^{N_\eta}$ the set of network weights, and $\{g_i(\eta)\}_{i=1}^{N_\eta} \equiv \left\{I_i^{(2)}(\eta)\right\}_{i=1}^{N_\eta}$ the set of RBFs, $I_i^{(1)}(\eta) = \int I_i^{(2)}(\eta)d\eta$, $I_i^{(0)}(\eta) = \int I_i^{(1)}(\eta)d\eta$, and c_1 and c_2 are the constants of integration. In Eq. 9 - Eq. 11, the function f can be used to represent the streamfunction, the vorticity or the temperature, while the variable η is employed to denote the (x,y) coordinate (Cartesian system), or (r,θ) coordinate (cylindrical system).

Evaluation of Eq. 9 - Eq. 11 at the grid nodes leads to

$$\widehat{\frac{d^2 f}{d\eta^2}} = \widehat{\mathscr{I}}^{(2)}\widehat{\alpha}, \tag{12}$$

$$\widehat{\frac{df}{d\eta}} = \widehat{\mathscr{I}}^{(1)}\widehat{\alpha}, \tag{13}$$

$$\widehat{f} = \widehat{\mathscr{I}}^{(0)}\widehat{\alpha}, \tag{14}$$

where the superscript $(.)$ is used to denote the order of the corresponding derivative function;

$$\widehat{\mathscr{I}^{(2)}} = \begin{bmatrix} I_1^{(2)}(\eta_1), & I_2^{(2)}(\eta_1), & \cdots, & I_{N_\eta}^{(2)}(\eta_1), & 0, & 0 \\ I_1^{(2)}(\eta_2), & I_2^{(2)}(\eta_2), & \cdots, & I_{N_\eta}^{(2)}(\eta_2), & 0, & 0 \\ \vdots & \vdots & \ddots & \vdots & \vdots & \vdots \\ I_1^{(2)}(\eta_{N_\eta}), & I_2^{(2)}(\eta_{N_\eta}), & \cdots, & I_{N_\eta}^{(2)}(\eta_{N_\eta}), & 0, & 0 \end{bmatrix};$$

$$\widehat{\mathscr{I}^{(1)}} = \begin{bmatrix} I_1^{(1)}(\eta_1), & I_2^{(1)}(\eta_1), & \cdots, & I_{N_\eta}^{(1)}(\eta_1), & 1, & 0 \\ I_1^{(1)}(\eta_2), & I_2^{(1)}(\eta_2), & \cdots, & I_{N_\eta}^{(1)}(\eta_2), & 1, & 0 \\ \vdots & \vdots & \ddots & \vdots & \vdots & \vdots \\ I_1^{(1)}(\eta_{N_\eta}), & I_2^{(1)}(\eta_{N_\eta}), & \cdots, & I_{N_\eta}^{(1)}(\eta_{N_\eta}), & 1, & 0 \end{bmatrix};$$

$$\widehat{\mathscr{I}^{(0)}} = \begin{bmatrix} I_1^{(0)}(\eta_1), & I_2^{(0)}(\eta_1), & \cdots, & I_{N_\eta}^{(0)}(\eta_1), & \eta_1, & 1 \\ I_1^{(0)}(\eta_2), & I_2^{(0)}(\eta_2), & \cdots, & I_{N_\eta}^{(0)}(\eta_2), & \eta_2, & 1 \\ \vdots & \vdots & \ddots & \vdots & \vdots & \vdots \\ I_1^{(0)}(\eta_{N_\eta}), & I_2^{(0)}(\eta_{N_\eta}), & \cdots, & I_{N_\eta}^{(0)}(\eta_{N_\eta}), & \eta_{N_\eta}, & 1 \end{bmatrix};$$

$$\widehat{\alpha} = \left(w_1, w_2, \cdots, w_{N_\eta}, c_1, c_2\right)^T;$$

and

$$\widehat{\frac{d^k f}{d\eta^k}} = \left(\frac{d^k f_1}{d\eta^k}, \frac{d^k f_2}{d\eta^k}, \cdots, \frac{d^k f_{N_\eta}}{d\eta^k}\right)^T, \qquad k = \{1,2\},$$

$$\widehat{f} = \left(f_1, f_2, \cdots, f_{N_\eta}\right)^T,$$

in which $d^k f_j/d\eta^k = d^k f(\eta_j)/d\eta^k$ and $f_j = f(\eta_j)$ with $j = \{1,2,\cdots,N_\eta\}$.
The relations between the RBF-coefficient space $\widehat{\alpha}$ and the physical space $\widehat{f}$ are given by

$$\begin{pmatrix} \widehat{f} \\ \widehat{e} \end{pmatrix} = \begin{bmatrix} \widehat{\mathscr{I}^{(0)}} \\ \widehat{\mathscr{K}} \end{bmatrix} \widehat{\alpha} = \widehat{\mathscr{C}}\widehat{\alpha}, \tag{15}$$

$$\widehat{\alpha} = \widehat{\mathscr{C}}^{-1} \begin{pmatrix} \widehat{f} \\ \widehat{e} \end{pmatrix}, \tag{16}$$

where $\widehat{e} = \widehat{\mathscr{K}}\widehat{\alpha}$ represents the extra information (e.g. normal derivative values at the two end-points) and $\widehat{\mathscr{C}}$ the conversion matrix.

Making use of Eq. 16, the values of f and its derivatives at an arbitrary point η on the grid line will be computed by

$$f(\eta) = \left(I_1^{(0)}(\eta), I_2^{(0)}(\eta), \cdots, I_{N_\eta}^{(0)}(\eta), \eta, 1\right) \widehat{\mathscr{C}}^{-1} \begin{pmatrix} \widehat{f} \\ \widehat{e} \end{pmatrix}, \tag{17}$$

$$\frac{\partial f(\eta)}{\partial \eta} = \left(I_1^{(1)}(\eta), I_2^{(1)}(\eta), \cdots, I_{N_\eta}^{(1)}(\eta), 1, 0\right) \widehat{\mathscr{C}}^{-1} \begin{pmatrix} \widehat{f} \\ \widehat{e} \end{pmatrix}, \tag{18}$$

$$\frac{\partial^2 f(\eta)}{\partial \eta^2} = \left(I_1^{(2)}(\eta), I_2^{(2)}(\eta), \cdots, I_{N_\eta}^{(2)}(\eta), 0, 0\right) \widehat{\mathscr{C}}^{-1} \begin{pmatrix} \widehat{f} \\ \widehat{e} \end{pmatrix}. \tag{19}$$

They can be rewritten in compact form

$$f(\eta) = \sum_{i=1}^{N_\eta} \varphi_i(\eta) f_i + \varphi_{N_\eta+1}(\eta) e_1 + \varphi_{N_\eta+2}(\eta) e_2, \tag{20}$$

$$\frac{\partial f(\eta)}{\partial \eta} = \sum_{i=1}^{N_\eta} \frac{\partial \varphi_i(\eta)}{\partial \eta} f_i + \frac{\partial \varphi_{N_\eta+1}(\eta)}{\partial \eta} e_1 + \frac{\partial \varphi_{N_\eta+2}(\eta)}{\partial \eta} e_2, \tag{21}$$

$$\frac{\partial^2 f(\eta)}{\partial \eta^2} = \sum_{i=1}^{N_\eta} \frac{\partial^2 \varphi_i(\eta)}{\partial \eta^2} f_i + \frac{\partial^2 \varphi_{N_\eta+1}(\eta)}{\partial \eta^2} e_1 + \frac{\partial^2 \varphi_{N_\eta+2}(\eta)}{\partial \eta^2} e_2, \tag{22}$$

where $\{\varphi_i\}_{i=1}^{N_\eta+2}$ is the set of IRBFN basis functions in the physical space.

One can take products of integrated RBFs in each direction as basis functions for the interpolation of f over the entire 2D domain. The IRBFN approximation is defined everywhere in the domain. It is easy to get the value of f at any point in the domain. Since the stream-function and vorticity transport equations are subject to Dirichlet boundary conditions only, the matrix $\widehat{\mathscr{K}}$ and the vector $\widehat{e}$ in Eq. 15 are simply set to null.

In the case of Cartesian coordinate system, approximate expressions for ψ and ω will take the form

$$\psi(x,y) = \sum_{i=1}^{N_x} \sum_{j=1}^{N_y} \varphi_i^{(x)}(x) \varphi_j^{(y)}(y) \psi_{i,j}, \tag{23}$$

$$\omega(x,y) = \sum_{i=1}^{N_x} \sum_{j=1}^{N_y} \varphi_i^{(x)}(x) \varphi_j^{(y)}(y) \omega_{i,j}, \tag{24}$$

where N_x and N_y are the numbers of grid lines in the y and x directions, respectively.

The energy equation is subject to both types of boundary conditions. Assume that Dirichlet and Neumann boundary conditions are prescribed on the two vertical and two horizontal walls, respectively. The integral approach allows one to incorporate Neumann boundary

conditions into the IRBFN approximations through integration constants. For each y grid line, the matrix $\widehat{\mathscr{K}}$ and the vector $\widehat{e}$ in Eq. 15 will become

$$\widehat{\mathscr{K}} = \begin{bmatrix} I_1^{(1)}(y_1), & I_2^{(1)}(y_1), & \cdots, & I_{N_y}^{(1)}(y_1), & 1, & 0 \\ I_1^{(1)}(y_{N_y}), & I_2^{(1)}(y_{N_y}), & \cdots, & I_{N_y}^{(1)}(y_{N_y}), & 1, & 0 \end{bmatrix},$$

$$\widehat{e} = \begin{pmatrix} \frac{\partial T_1}{\partial y} \\ \frac{\partial T_{N_y}}{\partial y} \end{pmatrix},$$

leading to

$$T(x,y) = \sum_{i=1}^{N_x} \varphi_i^{(x)}(x) \left(\sum_{j=1}^{N_y} \varphi_j^{(y)}(y) T_{i,j} + \varphi_{N_y+1}^{(y)}(y) \frac{\partial T_{i,1}}{\partial y} + \varphi_{N_y+2}^{(y)}(y) \frac{\partial T_{i,N_y}}{\partial y} \right). \tag{25}$$

In Eq. 23 - Eq. 25, $\psi_{i,j}$, $\omega_{i,j}$ and $T_{i,j}$ are the values of the ψ, ω and T variables at the intersection of the ith horizontal grid line and jth vertical grid line; the products $\varphi_i^{(x)}\varphi_j^{(y)}$ are usually referred to as the trial/basis/approximating functions; and $\partial T_{i,1}/\partial y$ and $\partial T_{i,N_y}/\partial y$ are nodal boundary derivative values.

In the case of cylindrical coordinates, the independent variables x and y in Eq. 23 - Eq. 25 will be replaced with r and θ.

3.2 Derivation of computation boundary conditions for the vorticity

This section presents a new treatment for the vorticity boundary condition in the discretisation of the $\psi-\omega-T$ formulation. Boundary conditions are over-specified for the streamfunction equation Eq. 1/Eq. 4, but under-specified for the vorticity transport equation Eq. 2/Eq. 5. There is the need to derive boundary conditions for the vorticity. In practice, the vorticity boundary values are usually derived from their definitions Eq. 1/Eq. 4 and boundary conditions for the streamfunction. Satisfaction of computational boundary conditions for the vorticity will have a strong influence on the accuracy of the final solution.

In the context of FDMs, Thom's formula and its variations have been widely used to obtain the vorticity boundary condition (e.g. [Roache (1982); Weinan and Liu (1996); Spotz (1998)]. These formulae are derived according to a local relation of the vorticity at the boundary. Although their implementations are quite straightforward, results by these formulae are observed to be uncertain in some cases (e.g. lower-order formulae may give better accuracy than high-order ones [Spotz (1998)]). Many other techniques such as the local radial point interpolation method (LRPIM) [Wu and Liu (2003)] and the local RBF-based differential quadrature method (RBF-DQM) [Shu, Ding, and Yeo (2003)] have also applied these boundary FD schemes, where grids near and including the boundary are required to be orthogonal.

In this study, two vorticity boundary schemes, which are global, are discussed. Taking into account the streamfunction boundary values (i.e. $\psi = 0$), expressions for the vorticity on the boundaries will reduce to

$$\omega = \frac{\partial^2 \psi}{\partial n^2}, \tag{26}$$

where n is the local direction normal to the wall. The two schemes presented below are different in the sense that $\partial\psi/\partial n$ is incorporated differently into the RHS of Eq. 26.

Approach 1: Consider a x grid line. Firstly, the RHS of Eq. 26 is expressed in terms of $\partial\psi/\partial x$

$$\widehat{\frac{\partial^2 \psi}{\partial x^2}} = \widehat{\mathscr{I}}^{(2)} \left(\widehat{\mathscr{I}}^{(1)}\right)^{-1} \widehat{\frac{\partial \psi}{\partial x}} = \widehat{\mathscr{I}}^{(2)} \left(\widehat{\mathscr{I}}^{(1)}\right)^{-1} \begin{pmatrix} \widehat{\frac{\partial \psi_{ip}}{\partial x}} \\ \frac{\partial \psi_1}{\partial x} \\ \frac{\partial \psi_{N_x}}{\partial x} \end{pmatrix}, \tag{27}$$

in which $\widehat{\partial \psi_{ip}/\partial x}$ and $\left(\partial\psi_1/\partial x, \partial\psi_{N_x}/\partial x\right)$ are the values of $\partial\psi/\partial x$ at the interior points $(x_2, \cdots, x_{N_x-1})$ and at the two boundary points (x_1, x_{N_x}), respectively. Secondly, the given values of $\partial\psi_1/\partial x$ and $\partial\psi_{N_x}/\partial x$ are substituted into Eq. 27, leading to

$$\widehat{\frac{\partial^2 \psi}{\partial x^2}} = \widehat{G}_x \widehat{\frac{\partial \psi_{ip}}{\partial x}} + \widehat{k}_x, \tag{28}$$

where $\widehat{G}_x$ is the known differentiation matrix in the physical space, and $\widehat{k}_x$ is the known vector whose components are functions of derivative boundary conditions. Thirdly, the first derivative values are written in terms of the nodal streamfunction values

$$\widehat{\frac{\partial \psi}{\partial x}} = \widehat{\mathscr{I}}^{(1)} \left(\widehat{\mathscr{I}}^{(0)}\right)^{-1} \widehat{\psi} = \widehat{\mathscr{I}}^{(1)} \left(\widehat{\mathscr{I}}^{(0)}\right)^{-1} \begin{pmatrix} \widehat{\psi}_{ip} \\ \psi_1 \\ \psi_{N_x} \end{pmatrix}, \tag{29}$$

in which $\widehat{\psi}_{ip}$ and (ψ_1, ψ_{N_x}) are the values of the streamfunction at the interior points and at the boundary points, respectively. Finally, by substituting Eq. 29 into Eq. 28, one will obtain computational boundary conditions for the vorticity, which are dependent on the nodal values of ψ at the interior points and at the two end-points of the grid line. For more details, the reader is referred to [Mai-Duy, Mai-Cao, and Tran-Cong (2007)].

Approach 2: Here, we propose that the incorporation of $\partial\psi/\partial n$ into the RHS of Eq. 26 is carried out with the help of the constants of integration. Consider a x grid line. Owing to the fact that the present coefficient vector is larger, one can add two extra equations representing

$\partial\psi_1/\partial x$ and $\partial\psi_{N_x}/\partial x$ to the conversion process

$$\begin{pmatrix} \widehat{\psi} \\ \frac{\partial\psi_1}{\partial x} \\ \frac{\partial\psi_{N_x}}{\partial x} \end{pmatrix} = \begin{bmatrix} \widehat{\mathscr{I}}^{(0)} \\ \widehat{\mathscr{K}} \end{bmatrix} \widehat{\alpha} = \widehat{\mathscr{C}}\widehat{\alpha}, \tag{30}$$

in which $\widehat{\mathscr{K}}$ is the matrix made up of the first and last rows of $\widehat{\mathscr{I}}^{(1)}$, i.e.

$$\widehat{\mathscr{K}} = \begin{bmatrix} I_1^{(1)}(x_1), & I_2^{(1)}(x_1), & \cdots, & I_{N_x}^{(1)}(x_1), & 1, & 0 \\ I_1^{(1)}(x_{N_x}), & I_2^{(1)}(x_{N_x}), & \cdots, & I_{N_x}^{(1)}(x_{N_x}), & 1, & 0 \end{bmatrix}.$$

It can be seen from Eq. 30 that, despite the presence of nodal derivative values, the approximate solution ψ is collocated at the whole set of centres on the grid line.

The second derivatives of ψ at the two boundary points can now be expressed in terms of the values of ψ at every point on the grid line and the values of $\partial\psi/\partial x$ at the two boundary points (x_1, x_{N_x})

$$\begin{pmatrix} \frac{\partial^2\psi_1}{\partial x^2} \\ \frac{\partial^2\psi_{N_x}}{\partial x^2} \end{pmatrix} = \widehat{\mathscr{D}}\widehat{\mathscr{C}}^{-1} \begin{pmatrix} \widehat{\psi} \\ \frac{\partial\psi_1}{\partial x} \\ \frac{\partial\psi_{N_x}}{\partial x} \end{pmatrix}, \tag{31}$$

where $\widehat{\mathscr{D}}$ is the sub-matrix of $\widehat{\mathscr{I}}^{(2)}$ (i.e. the first and last rows)

$$\widehat{\mathscr{D}} = \begin{bmatrix} I_1^{(2)}(x_1), & I_2^{(2)}(x_1), & \cdots, & I_N^{(2)}(x_1), & 0, & 0 \\ I_1^{(2)}(x_{N_x}), & I_2^{(2)}(x_{N_x}), & \cdots, & I_N^{(2)}(x_{N_x}), & 0, & 0 \end{bmatrix},$$

and $\widehat{\mathscr{C}}$ is defined in Eq. 30.

It can be seen that the IRBFN approximations for $\partial^2\psi/\partial x^2$ at the boundaries satisfy exactly the prescribed derivative boundary values. With Eq. 31, we can obtain the computational boundary conditions for the vorticity. On a y grid line, the process can be taken in a similar fashion. These boundary derivation processes are also applicable to the cylindrical coordinate system.

3.3 Galerkin discretisations of the PDEs

The discretisation process for Eq. 1 - Eq. 3 is similar to that for Eq. 4 - Eq. 6. For brevity, only the former is presented in detail here.

A distinguishing feature of the present method is that the IRBFNs approximations satisfy a priori not only the Dirichlet boundary conditions but also the Neumann boundary conditions. As a result, the Galerkin weighting process applied to Eq. 1 - Eq. 3 over the domain

Ω simply produces the following results (without the boundary-integral terms)

$$\int_\Omega W\left(\frac{\partial^2\psi}{\partial x^2}+\frac{\partial^2\psi}{\partial y^2}+\omega\right)d\Omega=0, \tag{32}$$

$$\int_\Omega W\frac{\partial\omega}{\partial t}d\Omega+\int_\Omega W\left(u\frac{\partial\omega}{\partial x}+v\frac{\partial\omega}{\partial y}\right)d\Omega-$$
$$\sqrt{\frac{Pr}{Ra}}\int_\Omega W\left(\frac{\partial^2\omega}{\partial x^2}+\frac{\partial^2\omega}{\partial y^2}\right)d\Omega-\int_\Omega W\frac{\partial T}{\partial x}d\Omega=0, \tag{33}$$

$$\int_\Omega W\frac{\partial T}{\partial t}d\Omega+\int_\Omega W\left(u\frac{\partial T}{\partial x}+v\frac{\partial T}{\partial y}\right)d\Omega-$$
$$\frac{1}{\sqrt{RaPr}}\int_\Omega W\left(\frac{\partial^2 T}{\partial x^2}+\frac{\partial^2 T}{\partial y^2}\right)d\Omega=0, \tag{34}$$

where W are the weighting/test functions which are taken from the set of trial functions (i.e. $W=\varphi_i^{(x)}\varphi_j^{(y)}$, where the values of i and j depend on the equation under consideration as will be shown later). Substituting Eq. 23 - Eq. 25 into Eq. 32 - Eq. 34, one will obtain the following three sets of algebraic equations

$$A_\psi\{\psi\}+M_\omega\{\omega\} = 0, \tag{35}$$

$$M_\omega\{\dot{\omega}\}+(KU_\omega+KV_\omega)\{\omega\}-\sqrt{\frac{Pr}{Ra}}A_\omega\{\omega\}+\{F_\omega\} = 0, \tag{36}$$

$$M_T\left\{\dot{T}\right\}+(KU_T+KV_T)\{T\}-\frac{1}{\sqrt{RaPr}}A_T\{T\} = 0, \tag{37}$$

where $\dot{\omega}=\partial\omega/\partial t$, $\dot{T}=\partial T/\partial t$, $\{\psi\}$ and $\{\omega\}$ the vectors of interior nodal values of ψ and ω, respectively, $\{T\}$ the vector of nodal values of T at the interior points and the Neumann boundary points, and

$$\left(A_\psi\right)_{i,j}=$$
$$\int_\Omega\varphi_m^{(x)}(x)\,\varphi_n^{(y)}(y)\left(\sum_{i=1}^{N_x}\sum_{j=1}^{N_y}\frac{\partial^2\varphi_i^{(x)}(x)}{\partial x^2}\varphi_j^{(y)}(y)+\sum_{i=1}^{N_x}\sum_{j=1}^{N_y}\varphi_i^{(x)}(x)\frac{\partial^2\varphi_j^{(y)}(y)}{\partial y^2}\right)d\Omega, \tag{38}$$

$$\left(M_\omega\right)_{i,j}=\int_\Omega\varphi_m^{(x)}(x)\,\varphi_n^{(y)}(y)d\Omega, \tag{39}$$

$$\left(KU_\omega\right)_{i,j}=u_{i,j}\int_\Omega\varphi_m^{(x)}(x)\,\varphi_n^{(y)}(y)\left(\sum_{i=1}^{N_x}\sum_{j=1}^{N_y}\frac{\partial\varphi_i^{(x)}(x)}{\partial x}\varphi_j^{(y)}(y)\right)d\Omega, \tag{40}$$

$$\left(KV_\omega\right)_{i,j}=v_{i,j}\int_\Omega\varphi_m^{(x)}(x)\,\varphi_n^{(y)}(y)\left(\sum_{i=1}^{N_x}\sum_{j=1}^{N_y}\varphi_i^{(x)}(x)\frac{\partial\varphi_j^{(y)}(y)}{\partial y}\right)d\Omega, \tag{41}$$

$$(A_\omega)_{i,j} = \int_\Omega \varphi_m^{(x)}(x)\,\varphi_n^{(y)}(y)\left(\sum_{i=1}^{N_x}\sum_{j=1}^{N_y}\frac{\partial^2\varphi_i^{(x)}(x)}{\partial x^2}\varphi_j^{(y)}(y)+\sum_{i=1}^{N_x}\sum_{j=1}^{N_y}\varphi_i^{(x)}(x)\frac{\partial^2\varphi_j^{(y)}(y)}{\partial y^2}\right)d\Omega, \quad (42)$$

$$\{F_\omega\}_{i,j} = \frac{\partial T_{i,j}}{\partial x}\int_\Omega \varphi_m^{(x)}(x)\,\varphi_n^{(y)}(y)d\Omega, \quad (43)$$

$$(KU_T)_{i,j} = u_{i,j}\int_\Omega \varphi_m^{(x)}(x)\,\varphi_l^{(y)}(y)\left(\sum_{i=1}^{N_x}\sum_{j=1}^{N_y}\frac{\partial\varphi_i^{(x)}(x)}{\partial x}\varphi_j^{(y)}(y)\right)d\Omega, \quad (44)$$

$$(KV_T)_{i,j} = v_{i,j}\int_\Omega \varphi_m^{(x)}(x)\,\varphi_l^{(y)}(y)\left(\sum_{i=1}^{N_x}\sum_{j=1}^{N_y}\varphi_i^{(x)}(x)\frac{\partial\varphi_j^{(y)}(y)}{\partial y}\right)d\Omega, \quad (45)$$

$$(A_T)_{i,j} = \int_\Omega \varphi_m^{(x)}(x)\,\varphi_l^{(y)}(y)\left(\sum_{i=1}^{N_x}\sum_{j=1}^{N_y}\frac{\partial^2\varphi_i^{(x)}(x)}{\partial x^2}\varphi_j^{(y)}(y)+\sum_{i=1}^{N_x}\sum_{j=1}^{N_y}\varphi_i^{(x)}(x)\frac{\partial^2\varphi_j^{(y)}(y)}{\partial y^2}\right)d\Omega, \quad (46)$$

$$(M_T)_{i,j} = \int_\Omega \varphi_m^{(x)}(x)\,\varphi_l^{(y)}(y)d\Omega, \quad (47)$$

in which $m = (2,3,...,N_x-1)$ (Dirichlet boundary conditions), $n = (2,3,...,N_y-1)$ (Dirichlet boundary conditions) and $l = (1,2,...,N_y)$ (Neumann boundary conditions). It is noted that this discretisation process leads to symmetric matrices.

The above volume integrals can be evaluated using repeated integrals, for which Gaussian points are employed along the grid lines.

3.4 Solution procedure

Due to the presence of convection terms (KU_ω, KV_ω, KU_T and KV_T) in the vorticity transport and energy equations, the resultant coupled sets of equations are nonlinear. We will adopt a time-marching approach, where the diffusion and convection terms are treated implicitly and explicitly, respectively. All equations involve the Laplacian term and their discrete form remains unchanged during the solution process. Moreover, the two matrices A_ψ and A_ω are identical. At each time level, the three equations are solved separately for efficiency purposes. The solution procedure can be summarised as follows.

1. Guess values of T, ψ, ω and their first-order spatial derivatives at time $t = 0$

2. Discretise spatial derivatives using 1D-IRBFNs, resulting in a high-order approximation scheme in space

3. Discretise time derivatives using Euler (forward difference) method, resulting in a first-order accurate scheme in time

4. Compute the boundary values for ω and the convective terms

5. Solve the energy equation Eq. 37 for T, subject to Dirichlet and Neumann conditions
   Solve the vorticity equation Eq. 36 for ω, subject to Dirichlet conditions
   Solve the streamfunction equation Eq. 35 for ψ, subject to Dirichlet conditions

6. Check to see whether the solution has reached a steady state

$$\frac{\sqrt{\sum_{i=1}^{N}\left(T_i^{(k)}-T_i^{(k-1)}\right)^2}}{\sqrt{\sum_{i=1}^{N}\left(T_i^{(k)}\right)^2}}<\varepsilon, \tag{48}$$

   where k is the time level and ε is a prescribed tolerance

7. If it is not satisfied, advance time step and repeat from step 3. Otherwise, stop the computation and output the results.

4 Numerical results

Several test problems are considered to validate the proposed technique. The first problem is for the treatment of the vorticity boundary condition, while the last two problems, namely natural convection in a square slot and a concentric annulus, are employed to study the accuracy of the method. For all numerical examples, uniform rectangular grids are used to represent the computational domain, and 1D-IRBFNs are implemented with the multiquadric (MQ) function

$$g_i(\eta)=\sqrt{(\eta-c_i)^2+a_i^2},$$

where c_i and a_i are the centre and the width/shape-parameter of the ith MQ-RBF. The MQ width is simply chosen to be the grid size.

4.1 Example 1 (vorticity boundary condition)

The two approaches, namely Approach 1 and Approach 2, for the treatment of boundary conditions for the vorticity are investigated here numerically by employing test problems

whose solutions are available in analytic form. Errors, which can be measured exactly, are computed using the relative discrete L_2 norm. Consider the following governing equations

$$\frac{\partial^2 \psi}{\partial x^2} + \frac{\partial^2 \psi}{\partial y^2} = -\omega, \tag{49}$$

$$\frac{\partial^2 \omega}{\partial x^2} + \frac{\partial^2 \omega}{\partial y^2} = f(x,y), \tag{50}$$

with two cases of boundary condition.

Homogeneous boundary conditions: For this case, the problem domain is a unit square ($\Omega = [0,1] \times [0,1]$) and the exact solution is taken as

$$\psi(x,y) = [1 - \cos(2\pi x)][1 - \cos(2\pi y)], \tag{51}$$

from which one can easily derive analytic forms for $\omega(x,y)$ and $f(x,y)$ on the RHSs of Eq. 49 and Eq. 50, respectively. Values of ψ and $\partial\psi/\partial n$ are all zero along the boundaries.

Numerical results for the solutions ψ and ω shown in Tab. 1 indicate that the proposed treatment (Approach 2) results in a significant improvement in accuracy. It can be seen that one order of magnitude better is generally observed for all grids used. For example, at a grid of 61×61, relative L_2 errors of ω are 2.0×10^{-4} and 3.9×10^{-5} for Approach 1 and Approach 2, respectively. Computational boundary conditions for the vorticity thus have a strong influence on the accuracy of the final solutions.

Inhomogeneous boundary conditions: For this case, the exact solution is taken as

$$\psi(x,y) = \sin(2\pi x)\cos(2y) - \cos(2\pi x)\sinh(2y), \tag{52}$$

on domain $\Omega = [-1,1] \times [-1,1]$. Results obtained are given in Tab. 2. Again, Approach 2 outperforms Approach 1 regarding accuracy. Approach 2 is recommended for use in practice. In the following, only Approach 2 is employed.

4.2 Example 2: Natural convection in a square slot

This problem is schematically defined in Fig. 1. The direction of gravity is parallel to the vertical walls. The problem is solved in Cartesian coordinates with the governing equations being Eq. 1 - Eq. 3. All walls are stationary, leading to $\psi = \partial\psi/\partial n = 0$ on the boundaries. The two horizontal walls are adiabatic (i.e. $\partial T/\partial y = 0$), while the two vertical walls are maintained at constant temperatures (i.e. $T = +0.5$ (left wall) and $T = -0.5$ (right wall)).

Numerical results for this problem are extensive. A range of *Ra* from 10^3 to 10^6 has been widely used for the validation of new numerical schemes. Davis (1983) provided finite-difference results which have been then often cited in the literature for comparison purposes. Later on, there are increased levels of interest for higher values of *Ra*, namely 10^7

and 10^8. Works reported include [Quéré (1991)] (the pseudo-spectral method), [Wan, Patnail, and Wei (2001)] (FEM), [Mayne, Usmani, and Crapper (2000, 2001)] ($h-$adaptive FEM), [Wan, Patnail, and Wei (2001)] (discrete singular convolution (DSC) method), [Sadat and Couturier (2000)] (meshless diffuse approximation method (DAM)), and [Kosec and Sarler (2007)] (mesh-free local RBF collocation method (RBFCM)). For this higher range, it has been generally observed that (i) the strength of boundary layers is significantly increased, (ii) convergence becomes much more difficult, and (iii) significant discrepancies in the Nusselt number occur in some cases (e.g. between the pseudo-spectral technique [Quéré (1991)] and the DSC method [Wan, Patnail, and Wei (2001)]).

The Galerkin-IRBFN method is employed to study this problem for $10^3 \leq Ra \leq 10^8$. Results are presented in the form of contour plots for ψ, ω and T and through the values of the following quantities

- The average Nusselt numbers on the vertical plane at $x = 0$ (left wall) and at $x = 1/2$ (middle cross-section), which are defined by

$$\begin{aligned} Nu_0 &= Nu(x=0,y), \\ Nu_{1/2} &= Nu(x=1/2,y), \end{aligned}$$

  in which

$$Nu(x,y) = \int_0^1 \left(uT - \frac{\partial T}{\partial x} \right) dy. \tag{53}$$

- The average Nusselt number throughout the cavity, which is defined by

$$\overline{Nu} = \int_0^1 Nu(x,y)dx. \tag{54}$$

- Maximum Nusselt number, Nu_{max}, on the plane $x = 0$ and its location
- Minimum Nusselt number, Nu_{min}, on the plane $x = 0$ and its location

It is noted that integrals Eq. 53 and Eq. 54 are computed here using Simpson's rule.

Results for Ra from 10^3 to 10^6 are presented in Tab. 3 and Fig. 2, and they are compared with those of Davis (1983). Denser grids are needed for higher values of Ra. When compared with low-order methods, the proposed technique requires relatively-coarse grids for the same level of accuracy. Results concerning the Nusselt numbers are shown in Tab. 3, where a fast convergence is observed. Fig. 2 shows the distributions of the temperature, streamfunction and vorticity fields, which are all in good qualitative agreement with the

benchmark results. For example, the three fields are skew-symmetric with respect to the centre of the slot, and the isotherms are nearly horizontal in the core flow as the Rayleigh number increases.

Results for Ra from 10^7 to 10^8 are presented in Tab. 4 and Fig. 3. Tab. 4 shows a comparison of the average Nusselt numbers between the present method and several other methods. It can be seen that there are significant discrepancies among various numerical techniques. For the case of $Ra = 10^7$, the DSC [Wan, Patnail, and Wei (2001)] and FEM [Manzari (1999)] produced the values of 13.86 and 13.99 for the average Nusselt number, while the pseudo-spectral [Quéré (1991)], FE [Wan, Patnail, and Wei (2001)], DA [Sadat and Couturier (2000)] and RBFCM [Kosec and Sarler (2007)] techniques yielded the following values: 16.523, 16.656, 16.59 and 16.92. The differences between the two groups are much wider for the case of $Ra = 10^8$: 23.67 for the DSC method, and (30.225, 31.486, 30.94, 32.12) for the second group. The Galerkin-IRBFN results are in close agreement with the second group, particularly with the pseudo-spectral technique [Quéré (1991)]. Variations of the local Nusselt number on the left and right walls are presented in Fig. 4. It is clearly shown that the proposed technique is able to capture very stiff changes of the local Nusselt number in the region close to the boundary. It can be seen from Fig. 3, the present contour plots for the streamfunction, vorticity and temperature variables look feasible when compared with those of the pseudo-spectral technique [Quéré (1991)]. Very thin boundary layers are formed at these high values of Ra. It is noted that iso-values used in these plots are the same as those used in [Quéré (1991)].

4.3 Example 3: Natural convection in a concentric annulus

Consider natural convection between two concentric cylinders that are separated by a distance L, the inner cylinder is heated and the outer cylinder cooled. Most cases have been reported with $Pr = 0.71$ and $L/D_i = 0.8$, in which D_i is the diameter of the inner cylinder. These conditions are also employed in the present work.

Since the flow is symmetric with respect to the vertical centreline, only half of the domain is needed for analysis. We employ cylindrical coordinates to solve this problem. Fig. 5 schematically shows the domain of analysis, the computational domain, a typical dicretisation used and the boundary conditions. The governing equations are employed in the form of Eq. 4 - Eq. 6, subject to the following boundary conditions

- on the symmetry plane: $\psi = 0, \ \omega = 0 \quad \text{and} \quad \partial T/\partial \theta = 0,$
- on the outer cylinder: $\psi = 0, \ \partial \psi/\partial r = 0 \quad \text{and} \quad T = 0,$
- on the inner cylinder: $\psi = 0, \ \partial \psi/\partial r = 0 \quad \text{and} \quad T = 1.$

This problem was studied in detail by various techniques. Among them are FDM [Kuehn and Glodstein (1976)], the differential quadrature (DQ) method [Shu (1999)] and the RBF-

based DQ method [Shu, Ding, and Yeo (2003); Shu and Wu (2007)] whose results are utilised here for comparison purposes.

We study this problem for the following values of *Ra*: $10^2, 10^3, 3\times10^3, 6\times10^3, 10^4, 5\times10^4$ and 7×10^4. Contour plots for the streamfunction and temperature are shown in Fig. 6, which look feasible in comparison with those of Kuehn and Glodstein (1976). When the Rayleigh number increases, the centre of rotation of the flows is observed to shift upward and the pattern of the temperature field becomes more complicated. At high values of *Ra* (5×10^4 and 7×10^4), thermal boundary layers appear near the lower portion of the inner cylinder and the top of the outer cylinder.

Another important result is the average equivalent conductivity denoted by $\overline{k}_{eq}$. This quantity is defined as the actual heat flux divided by the heat flux that would occur by pure conduction in the absence of the fluid motion:

$$\overline{k}_{eqi} = \frac{-\ln\left(R_o/R_i\right)}{\pi\left(R_o/R_i-1\right)}\int_0^\pi \frac{\partial T}{\partial r}d\theta, \tag{55}$$

for the inner cylinder, and

$$\overline{k}_{eqo} = \frac{-\left(R_o/R_i\right)\ln\left(R_o/R_i\right)}{\pi\left(R_o/R_i-1\right)}\int_0^\pi \frac{\partial T}{\partial r}d\theta, \tag{56}$$

for the outer cylinder, in which R_i and R_o are the radii of the inner and outer cylinders, respectively. Tab. 5 summarises the Galerkin-IRBFN results for various Rayleigh numbers using different grids and those of FDM [Kuehn and Glodstein (1976)] and DQM [Shu (1999)], which show good agreement between the methods for both the outer and inner cylinders.

5 Concluding remarks

We have successfully implemented a Galerkin-IRBFN method for the simulation of natural convection governed by the streamfunction-vorticity-temperature formulation in two dimensions. Its attractive features include: (i) easy implementation, (ii) effective treatment of the vorticity boundary condition, (iii) effective handling of the Neumann boundary condition, and (iv) ability to capture very thin boundary layers using relatively-coarse grids. Numerical experiments show that the proposed method achieves very high *Ra* solutions. It appears that this work is one of the earliest RBF reports which have successfully simulated the flow in a square slot at $Ra = 10^8$. This study further demonstrates the great potential of using RBFs in CFD.

Acknowledgement: This research is supported by Australia Research Council. D. Ho-Minh would like to thank the CESRC, FoES and USQ for a postgraduate scholarship. We would like to thank the reviewers for their helpful comments.

References

Atluri, S. N.; Han, Z. D.; Rajendran, A. M. (2004): A New Implementation of the Meshless Finite Volume Method, Through the MLPG "Mixed" Approach. *CMES:Computer Modeling in Engineering & Sciences*, vol. 6, pp. 491–514.

Davis, G. D. V. (1983): Natural convection of air in a square cavity: a bench mark numerical solution. *International Journal of Numerical Method Fluids*, vol. 3, pp. 249–264.

Divo, E.; Kassab, A. (2006): Iterative domain decomposition meshless method modeling of incompressible viscous flows and conjugate heat transfer. *Engineering Analysis with Boundary Elements*, vol. 30, pp. 465–478.

Ingber, M. S.; Chen, C. S.; Tanski, J. A. (2004): A mesh free approach using radial basis functions and parallel domain decomposition for solving three-dimensional diffusion equations. *International Journal for Numerical Methods in Engineering*, vol. 60, pp. 2183–2201.

Kansa, E. J. (1990): Multiquadrics - A scattered data approximation scheme with applications to computational fluid dynamics I. Surface approximations and partial derivative estimates. *Computers and Mathematics with Applications*, vol. 19, pp. 127–145.

Kansa, E. J.; Hon, Y. C. (2000): Circumventing the ill-conditioning problem with multiquadric radial basis functions: applications to elliptic partial differential equations. *Computers and Mathematics with Applications*, vol. 39, pp. 123–137.

Kosec, G.; Sarler, B. (2007): Solution of thermo-fluid problems by collocation with local pressure correction. *International Journal of Numerical Methods for Heat and Fluid Flow*, vol. 18, pp. 868–882.

Kosec, G.; Sarler, B. (2008): Local RBF Collocation Method for Darcy Flow. *CMES:Computer Modeling in Engineering & Sciences*, vol. 25, pp. 197–208.

Kuehn, T. H.; Glodstein, R. J. (1976): An experimental and theoretical study of natural convection in the annulus between horizontal concentric cylinders. *Journal of Fluids Mechanics*, vol. 74, pp. 695–719.

Ling, L.; Kansa, E. J. (2005): A least-squares preconditioner for radial basis functions collocation methods. *Advances in Computational Mathematics*, vol. 23, pp. 31–54.

Mai-Duy, N.; Mai-Cao, L.; Tran-Cong, T. (2007): Computation of transient viscous flows using indirect radial basis function networks. *CMES:Computer Modeling in Engineering & Sciences*, vol. 18, pp. 59–77.

Mai-Duy, N.; Tran-Cong, T. (2001): Numerical solution of differential equations using multiquadric radial basis function networks. *Neural Networks*, vol. 14, pp. 185–199.

Mai-Duy, N.; Tran-Cong, T. (2003): Approximation of function and its derivatives using radial basis function network methods. *Applied Mathematical Modelling*, vol. 27, pp. 197–220.

Mai-Duy, N.; Tran-Cong, T. (2007): A Cartesian-grid collocation method based on radial basis function networks for solving PDEs in irregular domains. *Numerical Methods for Partial Differential Equations*, vol. 23, pp. 1192–1210.

Mai-Duy, N.; Tran-Cong, T. (2009): An integrated-RBF technique based on Galerkin formulation for elliptic differential equation. *Engineering Analysis with Boundary Elements*, vol. 33, pp. 191–199.

Manzari, M. T. (1999): An explicit finite element algorithm for convective heat transfer problems. *International Journal of Numerical Methods for Heat and Fluid Flow*, vol. 9, pp. 860–877.

Mayne, D. A.; Usmani, A. S.; Crapper, M. (2000): h-Adaptive finite element solution of high Rayleigh number thermally driven cavity problem. *International Journal of Numerical Methods for Heat and Fluid Flow*, vol. 10, pp. 598–615.

Mayne, D. A.; Usmani, A. S.; Crapper, M. (2001): h-Adaptive finite element solution of unsteady thermally driven cavity problem. *International Journal of Numerical Methods for Heat and Fluid Flow*, vol. 11, pp. 172–194.

Mohammadi, M. H. (2008): Stabilized Meshless Local Petrov-Galerkin (MLPG) Method for Incompressible Viscous Fluid Flows. *CMES:Computer Modeling in Engineering & Sciences*, vol. 29, pp. 75–94.

Orsini, P.; Power, H.; Morvan, H. (2008): Improving Volume Element Methods by Meshless Radial Basis Function Techniques. *CMES:Computer Modeling in Engineering & Sciences*, vol. 23, pp. 187–208.

Quéré, P. L. (1991): Accuracy solutions to the square thermally driven cavity at high Rayleigh number. *Computers and Fluids*, vol. 20, pp. 29–41.

Roache, P. J. (1982): *Computational Fluid Dynamics*. Hermosa Publishers, Albuquerque, New Mexico.

Sadat, H.; Couturier, S. (2000): Performance and accuracy of meshless method for laminar natural convection. *Numerical Heat Transfer, Part B*, vol. 37, pp. 455–467.

Saitoh, T.; Hirose, K. (1989): High-accuracy benchmark solutions to natural convection in a square cavity. *Computation Mechanics*, vol. 4, pp. 417–427.

Sarler, B. (2005): A Radial Basis Function Collocation Approach in Computational Fluid Dynamics. *CMES:Computer Modeling in Engineering & Sciences*, vol. 7, pp. 185–194.

Schaback, R. (1995): Error estimates and condition numbers for radial basis function interpolation. *Advances in Computational Mathematics*, vol. 3, pp. 251–264.

Sellountos, E. J.; Sequeira, A. (2008): A Hybrid Multi-Region BEM / LBIE-RBF Velocity-Vorticity Scheme for the Two-Dimensional Navier-Stokes Equations. *CMES:Computer Modeling in Engineering & Sciences*, vol. 23, pp. 127–148.

Sellountos, E. J.; Sequeira, A.; Polyzos, D. (2009): Elastic transient analysis with MLPG(LBIE) method and local RBFs. *CMES:Computer Modeling in Engineering & Sciences*, vol. 41, pp. 215–242.

Shan, Y. Y.; Shu, C.; Lu, Z. L. (2008): Application of Local MQ-DQ Method to Solve 3D Incompressible Viscous Flows with Curved Boundary. *CMES:Computer Modeling in Engineering & Sciences*, vol. 25, pp. 99–114.

Shu, C. (1999): Application of differential quadrature method to simulate natural convection in a concentric annulus. *International Journal of Numerical Method Fluids*, vol. 30, pp. 977–993.

Shu, C.; Ding, H.; Yeo, K. (2003): Local radial basis function-based differential quadrature method and its application to solve two-dimensional incompressible Navier-Stokes equations. *Computer Methods in Applied Mechanics and Engineering*, vol. 192, pp. 941–954.

Shu, C.; Ding, H.; Yeo, K. S. (2005): Computation of incompressible Navier-Stokes equations by local RBF-based differential quadrature method. *CMES:Computer Modeling in Engineering & Sciences*, vol. 7, pp. 195–206.

Shu, C.; Wu, Y. L. (2007): Integrated radial basis functions-based differential quadrature method and its performance. *International Journal of Numerical Method Fluids*, vol. 53, pp. 969–984.

Spotz, W. F. (1998): Accuracy and performance of numerical wall boundary conditions for steady, 2D, incompressible streamfunction vorticity. *International Journal of Numerical Methods Fluid*, vol. 28, pp. 737–757.

Wan, D. C.; Patnail, B. S. V.; Wei, G. W. (2001): A new benchmark quality solution for the buoyancy-driven cavity by discrete singular convolution. *Numerical Heat Transfer, Part B*, vol. 40, pp. 199–228.

Wang, S. Y.; Lim, K. M.; Khoo, B. C.; Wang, M. Y. (2007): An Unconditionally Time-Stable Level Set Method and Its Application to Shape and Topology Optimization. *CMES:Computer Modeling in Engineering & Sciences*, vol. 21, pp. 1–40.

Wang, S. Y.; Wang, M. Y. (2006): Structural Shape and Topology Optimization Using an Implicit Free Boundary Parametrization Method. *CMES:Computer Modeling in Engineering & Sciences*, vol. 13, pp. 119–148.

Weinan, E.; Liu, J.-G. (1996): Vorticity boundary condition and related issues for Finite difference Schemes. *Journal of Computational Physics*, vol. 124, pp. 368–382.

Wu, Y. L.; Liu, G. R. (2003): A meshfree formulation of local radial point interpolation method (LRPIM) for incompressible flow simulation. *Computational Mechanics*, vol. 30, pp. 355–365.

Table 1: Example 1 (homogeneous boundary conditions): Relative L_2 errors of the solution ψ and ω. Notice that a(-b) means $a \times 10^{-b}$

	Errors of ω		Errors of ψ	
Grid	Approach 1	Approach 2	Approach 1	Approach 2
6×6	1.168(-1)	2.808(-2)	1.460(-1)	3.547(-2)
11×11	1.687(-2)	2.985(-3)	2.238(-2)	3.835(-3)
21×21	2.680(-3)	5.075(-4)	3.712(-3)	6.951(-4)
31×31	9.917(-4)	1.903(-4)	1.401(-3)	2.671(-4)
41×41	5.034(-4)	9.718(-5)	7.187(-4)	1.381(-4)
51×51	3.016(-4)	5.840(-5)	4.334(-4)	8.363(-5)
61×61	1.999(-4)	3.879(-5)	2.887(-4)	5.584(-5)

Table 2: Example 1 (inhomogeneous boundary conditions): Relative L_2 errors of the solution ψ and ω. Notice that a(-b) means $a \times 10^{-b}$

	Errors of ω		Errors of ψ	
Grid	Approach 1	Approach 2	Approach 1	Approach 2
6×6	6.096(-1)	1.845(-1)	2.137(0)	6.046(-1)
11×11	3.788(-2)	1.271(-2)	7.389(-2)	2.406(-2)
21×21	8.719(-3)	2.986(-3)	1.088(-2)	3.639(-3)
31×31	4.189(-3)	1.433(-3)	4.337(-3)	1.454(-3)
41×41	2.518(-3)	8.605(-4)	2.325(-3)	7.804(-4)
51×51	1.701(-3)	5.807(-4)	1.449(-3)	4.866(-4)
61×61	1.235(-3)	4.212(-4)	9.894(-4)	3.324(-4)

Table 3: Natural convection flow in a square slot: Comparison of the Galerkin-IRBFN results with the benchmark solution of Davis (1983) for $10^3 \leq Ra \leq 10^6$ and $Pr = 0.71$

	Characteristic values							
Ra	Grid size	$\overline{Nu}$	$Nu_{1/2}$	Nu_0	Nu_{max}	y	Nu_{min}	y
10^3	21×21	1.118	1.119	1.117	1.503	0.094	0.693	1
	[Davis (1983)]	1.118	1.118	1.117	1.505	0.092	0.692	1
10^4	21×21	2.254	2.258	2.242	3.514	0.149	0.592	1
	31×31	2.249	2.251	2.244	3.526	0.147	0.588	1
	41×41	2.247	2.248	2.244	3.529	0.146	0.587	1
	[Davis (1983)]	2.243	2.243	2.238	3.528	0.143	0.586	1
10^5	31×31	4.552	4.555	4.521	7.682	0.083	0.744	1
	41×41	4.539	4.540	4.519	7.689	0.086	0.736	1
	51×51	4.533	4.534	4.520	7.706	0.084	0.733	1
	61×61	4.529	4.530	4.521	7.712	0.083	0.731	1
	[Davis (1983)]	4.519	4.519	4.509	7.717	0.081	0.729	1
10^6	41×41	8.934	8.935	9.023	18.506	0.046	1.025	1
	51×51	8.899	8.900	8.872	17.794	0.041	1.008	1
	61×61	8.877	8.878	8.835	17.523	0.039	1.000	1
	71×71	8.864	8.865	8.827	17.458	0.040	0.993	1
	[Davis (1983)]	8.8	8.799	8.817	17.925	0.038	0.989	1

Table 4: Natural convection flow in a square slot: Comparison of the Galerkin-IRBFN results with those of other techniques for the two highest values of *Ra*

Ra	Technique	$\overline{Nu}$	$Nu_{1/2}$
10^7	Present study	16.661	16.661
	(Grid size: 91×91)		
	[Quéré (1991)]	16.523	16.523
	[Manzari (1999)]	13.99	
	[Sadat and Couturier (2000)]	16.59	
	[Wan, Patnail, and Wei (2001)] (FEM)	16.656	
	[Wan, Patnail, and Wei (2001)] (DSC)	13.86	
	[Kosec and Sarler (2007)]	16.92	
10^8	Present study	30.548	30.525
	(Grid size: 91×91)		
	[Quéré (1991)]	30.225	30.225
	[Sadat and Couturier (2000)]	30.94	
	[Wan, Patnail, and Wei (2001)] (FEM)	31.486	
	[Wan, Patnail, and Wei (2001)] (DSC)	23.67	
	[Kosec and Sarler (2007)]	32.12	

Table 5: Natural convection flow in an annulus: Convergence of the computed average equivalent conductivities with grid refinement for $10^2 \leq Ra \leq 7 \times 10^4$.

Ra	Grid size	Outer cylinder k_{eqo}	Inner cylinder k_{eqi}
10^2	11×11	1.000	1.000
	21×21	1.001	1.001
	[Kuehn and Glodstein (1976)]	1.002	1.000
	[Shu (1999)]	1.001	1.001
10^3	31×31	1.077	1.079
	41×41	1.078	1.080
	51×51	1.079	1.080
	[Kuehn and Glodstein (1976)]	1.084	1.081
	[Shu (1999)]	1.082	1.082
3×10^3	31×31	1.373	1.379
	41×41	1.378	1.384
	51×51	1.381	1.387
	[Kuehn and Glodstein (1976)]	1.402	1.404
	[Shu (1999)]	1.397	1.397
6×10^3	31×31	1.676	1.689
	41×41	1.684	1.697
	51×51	1.690	1.701
	[Kuehn and Glodstein (1976)]	1.735	1.736
	[Shu (1999)]	1.715	1.715
10^4	41×41	1.937	1.959
	51×51	1.945	1.964
	61×61	1.953	1.967
	[Kuehn and Glodstein (1976)]	2.005	2.010
	[Shu (1999)]	1.979	1.979
5×10^4	41×41	2.794	2.938
	51×51	2.835	2.943
	61×61	2.866	2.946
	[Kuehn and Glodstein (1976)]	2.973	3.024
	[Shu (1999)]	2.958	2.958
7×10^4	41×41	2.970	3.174
	51×51	3.027	3.180
	61×61	3.070	3.182
	[Kuehn and Glodstein (1976)]	3.226	3.308

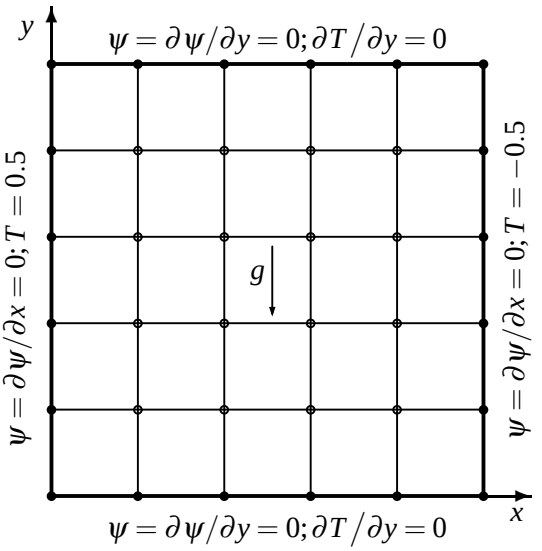

Figure 1: Natural convection flow in a square slot: geometry definition, boundary conditions and discretisation

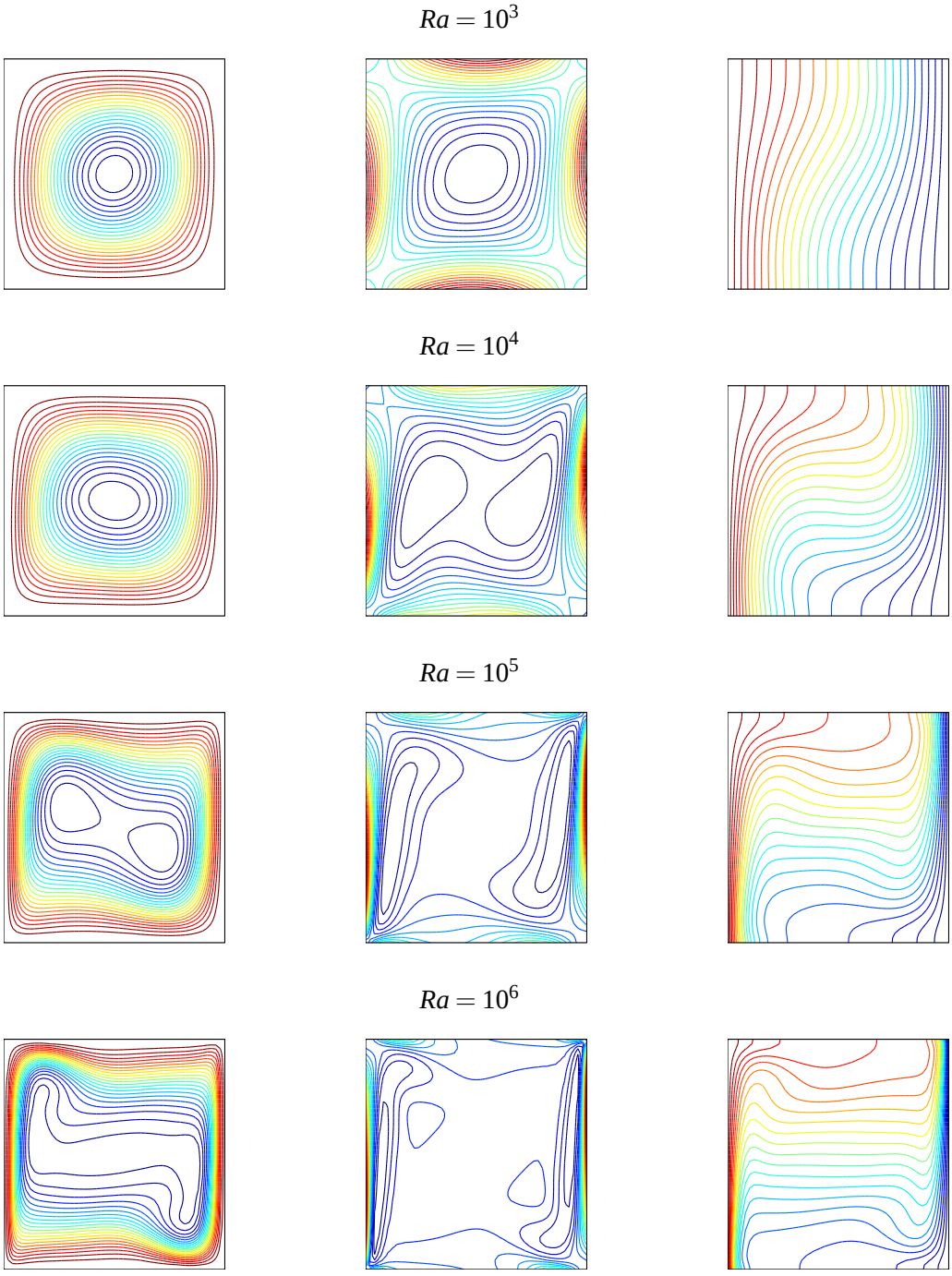

Figure 2: Natural convection flow in a square slot: Contour plots for the ψ (left), ω (middle) and T (right) variables at four different values of Ra using a grid of 51×51. Each plot draws 21 contour lines whose values vary uniformly from the minimum to maximum values.

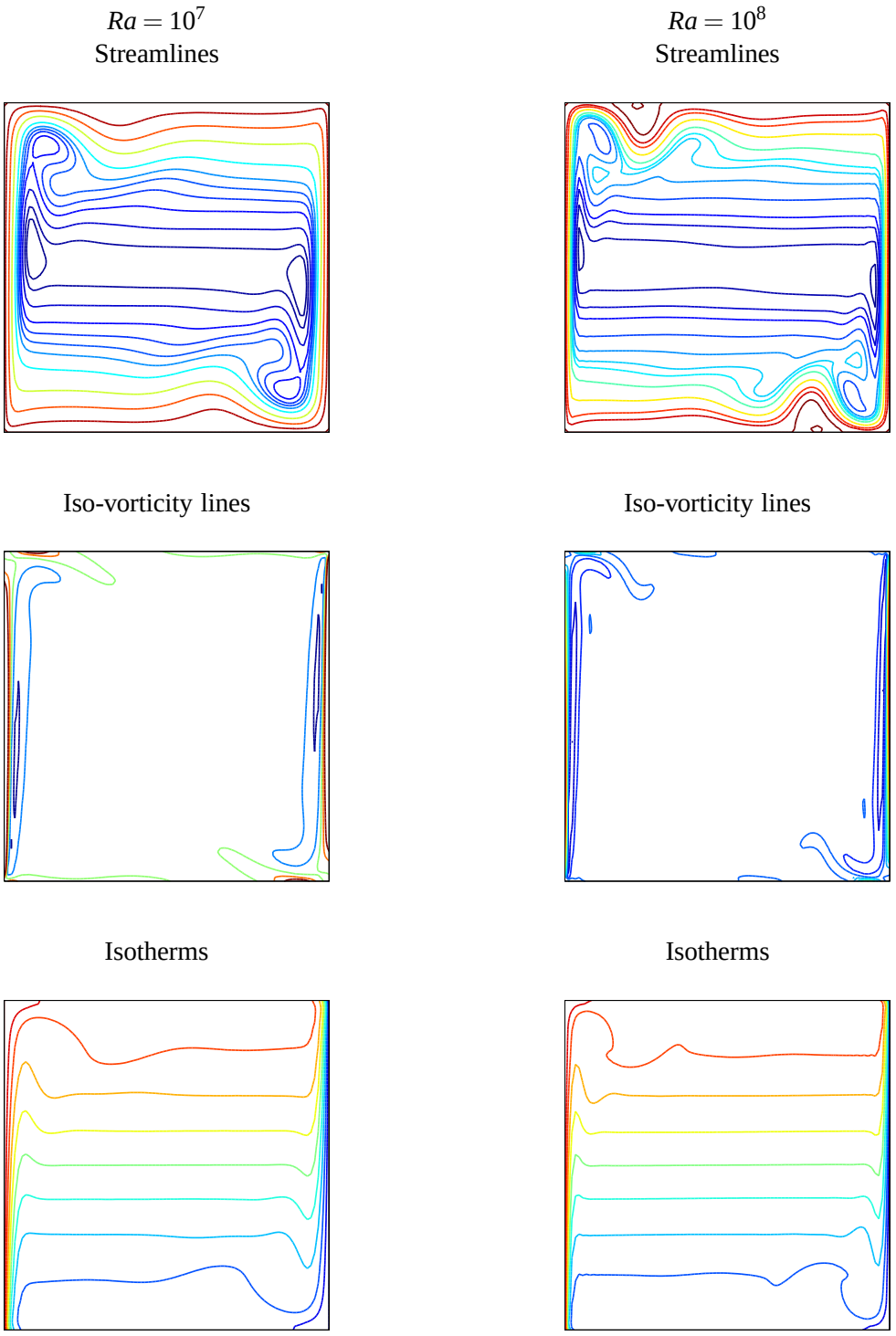

Figure 3: Natural convection flow in a square slot: Contour plots for the ψ, ω and T variables at $Ra = 10^7$ and $Ra = 10^8$ using a grid of 91×91. Iso-values used in these plots are the same as those in [Quéré (1991)].

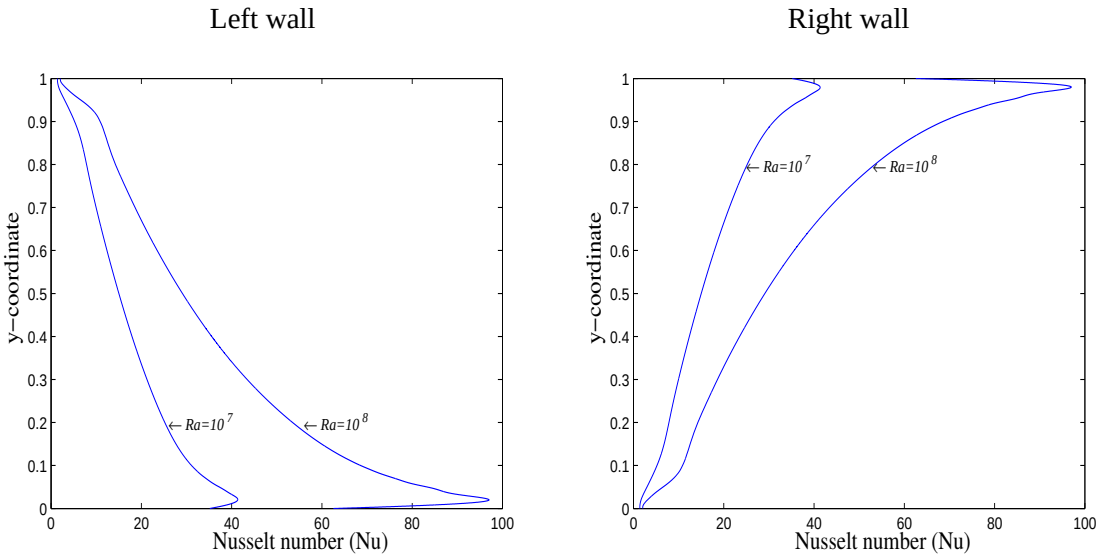

Figure 4: Natural convection flow in a square slot: Variations of the local Nusselt number along the left and right walls.

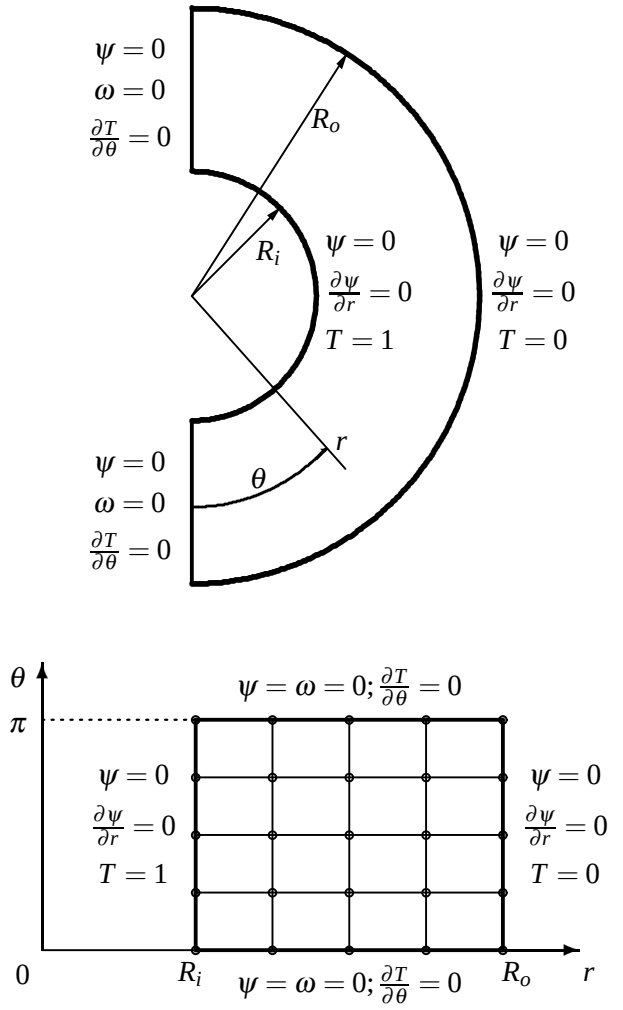

Figure 5: Natural convection flow in an annulus: domain of interest (upper figure), computational domain (lower figure), boundary conditions and discretisation

$Ra = 10^3$

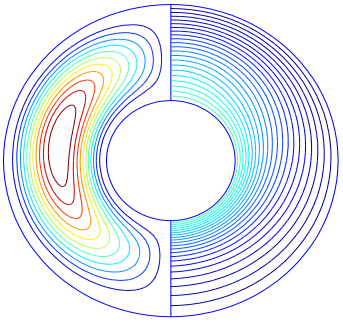

$Ra = 3 \times 10^3$

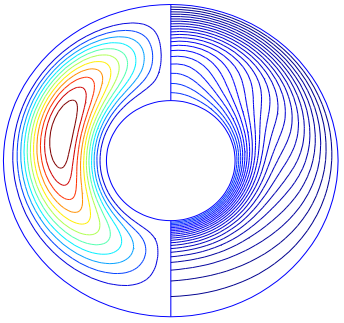

$Ra = 6 \times 10^3$

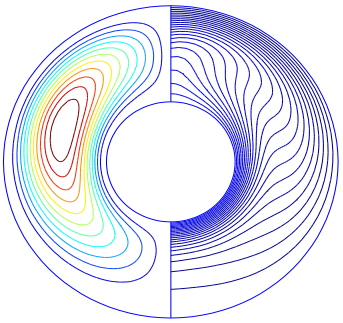

$Ra = 10^4$

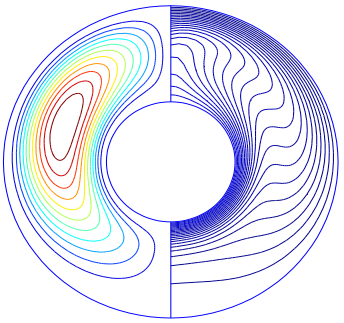

$Ra = 5 \times 10^4$

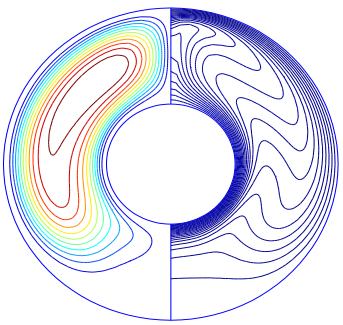

$Ra = 7 \times 10^4$

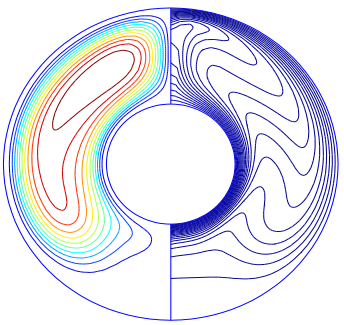

Figure 6: Natural convection flow in an annulus: Contour plots for the ψ (left) and T (right) variables for six different Rayleigh numbers using a grid of 51×51.